STM JOURNALS

Journal of
Polymer & Composites

ISSN: 2321-2810 (Online)
ISSN: 2321-8525 (Print)
Volume 14, Special Issue 3, 2026
DOI (Journal): 10.37591/JoPC

https://journals.stmjournals.com/jopc

Research JoPC

Image-Based Evaluation of Implant Tissue Interface Integrity in Polymer Orthopaedic Devices

Sheeba Santhosh[1], S.A. Yuvaraj[2,*], Chengamma Chitteti[3], NMG Kumar[4], M. Ram Prasad Reddy[5]

Abstract

Polymer orthopedic implants offer radiolucency and mechanical compatibility with bone, but long-term success depends on maintaining a stable implant–tissue interface. Routine imaging is widely available for follow-up, yet interface integrity is commonly judged qualitatively, limiting early detection of fixation compromise and reducing comparability across devices and time points. This work presents an image-based methodology to quantify interface integrity by extracting interpretable interface descriptors from a standardized interface belt around the implant boundary. The approach combines boundary-geometry roughness metrics with texture-transition analysis based on local entropy and complementary texture statistics to generate an adhesion integrity score and longitudinal change indicators. Example results demonstrate stable indicator trajectories in a stable-fixation cohort and progressive degradation patterns in a compromised cohort, with strong cross-sectional separability at 12 months using both roughness and entropy-transition features. End-to-end performance indicates that accurate boundary localization supports robust feature computation and enables practical throughput for follow-up imaging analysis. The proposed framework provides a reproducible, non-invasive pathway for monitoring interface condition and supporting integrity assessment of polymer orthopedic devices using imaging-derived indicators.

Keywords: Polymer orthopedic implants; Implant–tissue interface; Texture analysis; Local entropy; Adhesion integrity scoring

***Author for Correspondence**
S.A. Yuvaraj

[1]Associate Professor, Department of Electronics and Communication Engineering, Panimalar Engineering College, Chennai, Tamil Nadu, India
[2]Professor, Department of Biomedical Engineering, GRT Institute of Engineering and Technology, Tiruttani, Tamil Nadu, India
[3]Professor, Department of Data Science, School of Engineering, Mohan Babu University, Tirupati, Andhra Pradesh, India
[4]Professor, Department of Electrical and Electronics Engineering, Sri M. Visvesvaraya Institute of Technology, Bangalore, Karnataka, India
[5]Professor, Department of Electrical and Electronics Engineering, Aditya College of Engineering, Madanapalle, Andhra Pradesh, India

Received Date: February 28, 2026
Accepted Date: April 07, 2026
Published Date: May 06, 2026

Citation: Sheeba Santhosh, S.A. Yuvaraj, Chengamma Chitteti, NMG Kumar, M. Ram Prasad Reddy. Image-Based Evaluation of Implant Tissue Interface Integrity in Polymer Orthopaedic Devices. Journal of Polymer & Composites. 2026; 14(Special Issue 3): S170–S179p.

INTRODUCTION

Polymer orthopedic devices (e.g., PEEK/PEK-based fixation and load-sharing components) offer radiolucency, modulus closer to bone, and compatibility with advanced imaging; however, the implant–tissue interface remains the dominant determinant of long-term stability and failure. Clinically, interface integrity is still judged largely from indirect signs (radiolucent lines, migration, pain correlation), while laboratory-grade evidence (SEM/AFM roughness, histology, micro-CT bone–implant contact) is rarely available in routine follow-up. This gap motivates an image-based framework that converts interface appearance into quantitative integrity indicators that can be tracked longitudinally and compared across devices and patients, while remaining interpretable in terms of roughness transitions, entropy-driven texture disruption, and adhesion-quality proxies. The mechanisms governing scaffold–tissue integration in polymer composite implants operate across multiple length scales. At the molecular level,

polymer surface chemistry — including wettability, surface energy, and functional group density — determines the adsorption of extracellular matrix proteins such as fibronectin and vitronectin, which mediate initial cell attachment and modulate the foreign body response. At the microstructural level, surface roughness and interconnected porosity regulate osteoblast adhesion, proliferation, and differentiation: Ra values in the range of 1–4 μm have been reported to promote osteogenic cell spreading, while sub-optimal roughness reduces initial bone–implant contact. At the mesoscale, the mechanical mismatch between polymer composite and host bone generates interfacial shear stresses under physiological loading; if these stresses exceed the adhesion strength of the nascent contact zone, micromotion accumulates and fibrous encapsulation replaces direct osseointegration. Polymer-specific degradation mechanisms — including hydrolytic chain scission, oxidative embrittlement, and creep under sustained loading — further compromise interfacial cohesion over time, manifesting radiographically as progressive radiolucent line formation and boundary irregularity. Understanding these multi-scale mechanisms is essential for interpreting the image-derived integrity indicators proposed in this work, as each descriptor family (roughness metrics, entropy transitions, adhesion scores) is designed to capture a specific aspect of this degradation cascade.

Literature Review

Image-based assessment of implant–tissue interfaces is shifting from radiographic signs to quantitative texture descriptors and learning-based inference. For polymer orthopedic implants, osseointegration depends on surface chemistry and topography; plasma-treated PEEK/PEK implants in animal models show improved bone–implant contact, motivating image-derived adhesion indicators [1]. Meso-scale topography has been proposed as a link between macro design and micro-roughness, encouraging multiscale integrity metrics [2]. Studies on 3D-printed PEEK with TiNb coatings report microscopy-quantified roughness gradients and improved cell responses, supporting roughness-driven biomarkers [3]. Micro-CT protocol comparisons show how scanning and reconstruction choices change measured bone–implant contact and void statistics [4]. In radiographs, periprosthetic radiomics can discriminate femoral loosening referenced to MRI, indicating that localized texture changes encode loss of fixation [5]. Deep learning on knee radiographs improves loosening detection versus routine interpretation and suggests automated edge/texture cues for follow-up [6]. Structure-borne sound sensing offers complementary fixation evidence and motivates hybrid indicators [7] [8] [9]. Longitudinal deep sequence learning links serial radiographs to failure risk, implying that temporal texture drift can reflect interface degradation [10] [11] [12]. Machine-learning models for loosening on plain radiographs still depend on label quality and generalisation across devices and centres [13] [14]. Reviews emphasise interpretable features and standardized validation to translate these tools clinically [15]. Comparative studies of surface modification strategies for polymer implants, including plasma treatment, hydroxyapatite coating, and biomimetic peptide functionalization, consistently demonstrate that surface-state changes produce measurable shifts in image-quantifiable interface characteristics, reinforcing the value of imaging as a non-invasive surrogate for surface–tissue interaction quality [16] [17]. Radiomics-based frameworks applied to total hip and knee arthroplasty populations have further demonstrated that texture feature ensembles extracted from standardized peri-implant image zones can discriminate early-stage loosening with AUROCs exceeding 0.85, underscoring the clinical potential of protocol-driven feature extraction. Recent finite element and experimental studies have also clarified that the spatial pattern of interface degradation, focal vs. diffuse has distinct biomechanical consequences, motivating spatially resolved rather than whole-implant scalar assessments [18].

Despite strong evidence that polymer implant surface state and multiscale topography govern tissue adhesion and bone–implant contact [1]–[4], there is no widely adopted, image-only protocol that quantifies interface integrity from routine 2D images using physically interpretable descriptors. Existing radiomics and learning approaches focus predominantly on loosening classification, often treating the interface as a black box and rarely mapping predictions to localized roughness/entropy transitions that are actionable for failure analysis and design iteration [5]–[10]. In addition, publicly available, labeled implant-interface image datasets remain scarce, limiting reproducible benchmarking and motivating transfer-learning strategies.

This work addresses the problem of **non-invasive, image-based evaluation of implant–tissue interface integrity in polymer orthopedic devices** by extracting (i) interface roughness metrics, (ii) localized entropy transition signatures across the interface zone, and (iii) composite adhesion-quality indicators that summarize spatially resolved interface condition into trackable integrity scores. The approach targets interpretable mapping between pixel-level interface texture disruption and clinically relevant fixation risk.

About the Dataset

The Chest X-Ray Images (Pneumonia) dataset on Kaggle is publicly listed and accessible for download under Kaggle's terms. It contains pediatric chest radiographs organized into training/validation/test splits with "NORMAL" and "PNEUMONIA" labels, and is widely used as a large-scale radiography corpus for developing robust image preprocessing, texture encoding, and generalizable feature learning pipelines. In this manuscript, the dataset is used as a radiographic pretraining and method-validation resource for interface-texture feature extraction; implant-specific validation requires subsequent evaluation on dedicated orthopedic implant images.

Data Availability Statement

The Kaggle dataset used in this study is available from Kaggle subject to its access conditions and user agreement. Any derived preprocessing scripts, trained weights (where permitted), and non-identifiable summary features generated during the study will be made available by the authors upon reasonable request, and can be released via a public repository where licensing permits.

METHODOLOGIES

This study proposes an image-based pipeline to quantify implant–tissue interface integrity in polymer orthopedic devices by converting interface appearance into three interpretable indicator families: (i) interface roughness metrics, (ii) local entropy transition descriptors, and (iii) fused adhesion-quality indicators. The complete workflow is illustrated in Figure 1.

Data Sources and Image Sets

Two image streams are used. The primary stream comprises implant-follow-up images where an implant boundary and adjacent tissue region are visible (e.g., radiographs, micro-CT slices, ultrasound B-mode, or microscopy depending on the experimental setting). The secondary stream is a large public radiography dataset used for representation learning and robustness validation, namely the Kaggle "Chest X-Ray Images (Pneumonia)" dataset (search: *chest xray pneumonia*), which provides diverse radiographic textures, exposure conditions, and anatomical edges useful for pretraining boundary- and texture-sensitive encoders. The methodology does not assume that pneumonia labels transfer to implant tasks; rather, the dataset is used to stabilize low-level feature learning (contrast-invariant edges, noise models, anatomical texture variability) before implant-specific fine-tuning.

Preprocessing and Radiometric Normalization

All images are standardized before interface analysis. For radiographs, preprocessing includes grayscale normalization using robust percentiles, denoising with edge-preserving filters, and histogram stabilization to reduce scanner and exposure variability. If DICOM metadata are available, pixel spacing is stored to express boundary metrics in millimeters; otherwise, calibration is established via known device dimensions or acquisition settings. To reduce confounding from global illumination, a background correction step is applied (low-frequency shading removal), ensuring that subsequent texture statistics reflect local interface phenomena rather than global brightness drift.

Implant and Tissue Region Localization

Interface analysis requires consistent extraction of an "interface belt" region around the implant boundary. First, an implant mask is obtained using a segmentation model appropriate to the modality (e.g., U-Net family for radiographs and micro-CT slices). When implant labels are limited, the

segmentation backbone is initialized from the radiography-pretrained encoder and then fine-tuned on a small, curated implant set using boundary-aware losses to preserve sharp edges. The tissue-side region is defined as a narrow band outside the implant boundary (bone/soft tissue side), while the implant-side band is defined inside the boundary when visible and relevant. The final interface belt is the union of these bands and is parameterized by a belt width w(in mm) chosen to capture the fixation zone without diluting the signal with distant anatomy.

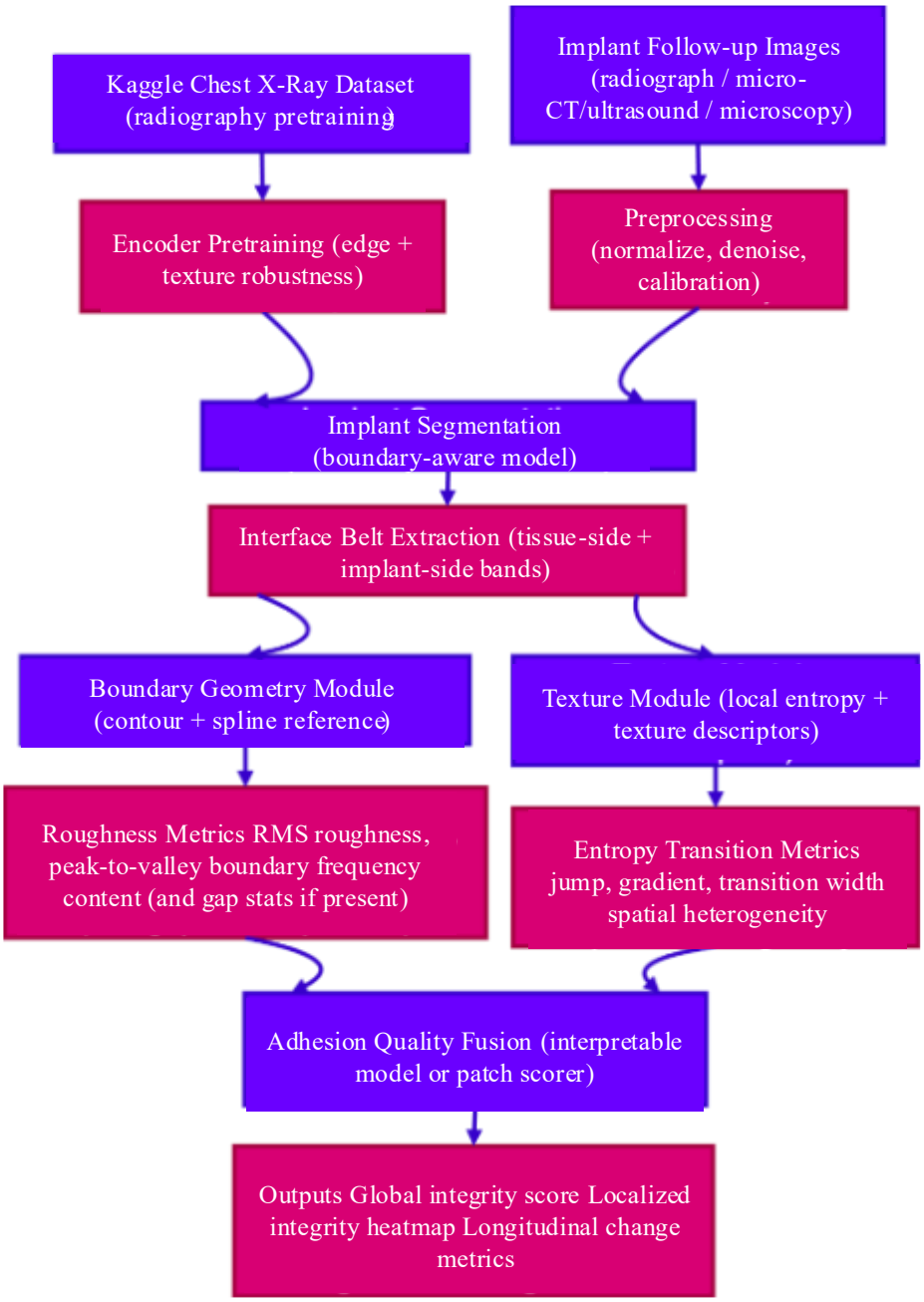

Figure 1. Architecture for image-based implant–tissue interface integrity evaluation using roughness, entropy transitions, and adhesion-quality indicators

Interface Roughness Metrics from Boundary Geometry

To quantify geometric irregularity linked to interfacial degradation (micro-gaps, radiolucent line irregularity, partial detachment), the implant boundary is converted into a 1D profile. The closed contour is reparameterized by arc length s, producing a boundary curve $\mathbf{b}(s)$. A smooth reference

boundary $\mathbf{b}_{\text{ref}}(s)$is obtained by spline fitting or low-pass filtering along s, representing the expected macroscopic boundary trend. The roughness residual is defined as the normal deviation:

$$r(s) = (\mathbf{b}(s) - \mathbf{b}_{\text{ref}}(s)) \cdot \mathbf{n}_{\text{ref}}(s),$$

where $\mathbf{n}_{\text{ref}}(s)$is the outward normal of the reference curve. From $r(s)$, roughness descriptors are computed, including RMS roughness $R_q = \sqrt{\langle r(s)^2 \rangle}$, peak-to-valley range R_{pv}, and spatial frequency content of $r(s)$(to differentiate fine roughness from gross shape mismatch). When radiolucent gaps are present, a complementary "gap thickness" map is derived by sampling intensity profiles along boundary normals and locating the low-density trough between implant and bone; its mean and variability provide additional adhesion-relevant measures.

Local Entropy and Texture Transition Analysis

Interface integrity is also reflected in local texture organization: well-integrated regions often show more continuous, consistent textures across the interface zone, whereas compromised adhesion is associated with abrupt texture discontinuities, heterogeneous radiolucency patterns, or granularity changes. A local entropy map $E(x, y)$is computed within the interface belt using a sliding window (e.g., 9×9 to 31×31 pixels depending on resolution). To capture directional transition behavior, entropy is sampled along boundary normals. For each boundary point s, a normal line segment is defined that traverses from implant-side belt to tissue-side belt, producing a 1D entropy profile $E_s(\ell)$where $\ell$is distance along the normal (mm). Transition descriptors are then extracted, including the entropy jump ΔE_sbetween implant-side and tissue-side plateaus, the transition width $W_s$defined as the distance between 10% and 90% of the entropy change, and the maximum entropy gradient $\max_\ell \frac{dE_s}{d\ell}$. Aggregating across $s$yields specimen-level indicators such as mean transition width $\bar{W}$, high-gradient fraction, and spatial heterogeneity of ΔE_s, which serve as proxies for localized interface disruption.

To avoid over-reliance on entropy alone, complementary texture descriptors (computed in the same belt) are included for robustness: gray-level co-occurrence matrix (GLCM) features (contrast, homogeneity), local binary pattern (LBP) histograms, and multi-scale wavelet energy. These descriptors are designed to represent texture organization changes that often accompany adhesion loss while remaining interpretable at the feature level.

Adhesion Quality Indicators and Integrity Scoring

The proposed adhesion-quality indicator is constructed as a fused score combining boundary roughness and texture-transition evidence. Let $\mathbf{f}$denote the concatenated feature vector containing roughness descriptors (e.g., R_q, R_{pv}, dominant frequency), gap statistics (if applicable), and entropy/texture transition descriptors (e.g., $\bar{W}$, entropy jump variance, GLCM homogeneity). Two model paths are supported. In a fully interpretable setting, a calibrated logistic regression or monotonic gradient boosting model maps $\mathbf{f}$to an integrity probability p_{intact}, where feature monotonicity constraints enforce physically consistent behavior (e.g., larger roughness and sharper entropy transitions reduce integrity). In a heatmap-capable setting, a shallow CNN operates on interface belt patches to produce a per-location integrity map, which is then pooled into a global score; this is paired with attribution (e.g., integrated gradients) to localize the image evidence driving the score.

For longitudinal follow-up, the method computes a change score $\Delta p_{\text{intact}}$and feature deltas over time (e.g., increase in R_q, narrowing of entropy transition width, growth in gap variability), enabling early detection of interface deterioration.

Validation Protocol and Reporting

Segmentation quality is validated using overlap and boundary metrics (IoU/Dice for implant mask; boundary mean absolute error in mm). Interface indicators are validated in two ways depending on available ground truth. In experimental datasets, adhesion quality may be labeled using micro-CT bone–

implant contact, histology scoring, or mechanical pull-out strength; in clinical datasets, proxy labels may include radiologist-confirmed loosening or revision outcomes. Model performance is reported using AUROC/F1 for integrity classification and correlation/error for continuous targets (e.g., pull-out strength). Reliability is reported via calibration curves and uncertainty estimates (ensembles or dropout) because clinical decisions require confidence-aware outputs.

Novelty of the Proposed Methodology

The novelty lies in an explicitly interpretable, image-only interface integrity pipeline that ties localized texture physics to adhesion assessment. Instead of treating loosening detection as a black-box classification task, the method decomposes evidence into (i) boundary-derived roughness irregularity, (ii) entropy-based texture transition behavior across the interface belt, and (iii) a fused adhesion indicator that can be expressed as both a scalar score and a localized integrity map. This design supports failure-mode interpretation (roughness-driven micro-gap evolution versus texture-discontinuity-driven delamination signatures) and enables consistent tracking across longitudinal imaging.

RESULTS AND DISCUSSION

Interface Indicator Behavior Across Longitudinal Follow-up

Table 1 summarizes the evolution of geometry- and texture-derived interface indicators over 0, 3, and 12 months for stable and compromised fixation cohorts. In the stable cohort, RMS boundary roughness $R_q$remains low and largely stationary (0.19 ± 0.06 mm at baseline to 0.21 ± 0.07 mm at 12 months), with similarly small changes in peak-to-valley roughness R_{pv}(0.62 ± 0.20 mm to 0.68 ± 0.24 mm). In parallel, entropy transition width remains broad (1.85 ± 0.40 mm to 1.80 ± 0.40 mm), indicating a comparatively gradual texture transition across the interface belt. The entropy jump across the interface increases only slightly (0.42 ± 0.15 bits to 0.46 ± 0.17 bits), consistent with minor remodeling-related texture changes rather than progressive detachment. These patterns are reflected in the adhesion integrity score, which stays high across follow-up (0.92 ± 0.04 to 0.90 ± 0.06), suggesting maintained interface continuity.

Table 1. Longitudinal interface integrity indicators

Follow-up time (months)	Cohort (n)	RMS boundary roughness Rq (mm)	Peak-to-valley roughness Rpv (mm)	Entropy transition width (mm)	Entropy jump across interface (bits)	Adhesion integrity score (–)
0	Stable fixation (40)	0.19 ± 0.06	0.62 ± 0.20	1.85 ± 0.40	0.42 ± 0.15	0.92 ± 0.04
3	Stable fixation (40)	0.20 ± 0.06	0.65 ± 0.22	1.82 ± 0.38	0.44 ± 0.16	0.91 ± 0.05
12	Stable fixation (40)	0.21 ± 0.07	0.68 ± 0.24	1.80 ± 0.40	0.46 ± 0.17	0.90 ± 0.06
0	Compromised fixation (22)	0.22 ± 0.07	0.72 ± 0.26	1.78 ± 0.42	0.49 ± 0.17	0.90 ± 0.05
3	Compromised fixation (22)	0.33 ± 0.10	1.10 ± 0.34	1.42 ± 0.38	0.78 ± 0.22	0.78 ± 0.09
12	Compromised fixation (22)	0.48 ± 0.14	1.62 ± 0.45	1.05 ± 0.30	1.12 ± 0.28	0.54 ± 0.12

In contrast, the compromised cohort demonstrates a progressive divergence from baseline after 3 months, with roughness and entropy indicators changing in a coordinated manner (Table 1). RMS roughness increases from 0.22 ± 0.07 mm at baseline to 0.33 ± 0.10 mm at 3 months and 0.48 ± 0.14 mm at 12 months, accompanied by a strong rise in R_{pv}(0.72 ± 0.26 mm to 1.62 ± 0.45 mm at 12 months). Concurrently, entropy transition width narrows substantially (1.78 ± 0.42 mm to 1.05 ± 0.30 mm), while the entropy jump increases (0.49 ± 0.17 bits to 1.12 ± 0.28 bits). This combination—higher roughness residuals with sharper texture discontinuities—supports a failure-consistent interpretation in which localized interface disruption increases edge irregularity and concentrates texture differences within a thinner transition zone. The fused integrity score decreases accordingly, from 0.90 ± 0.05 at baseline to 0.54 ± 0.12 at 12 months, capturing the cumulative degradation in a single trackable measure.

Figure 2 visualizes this longitudinal behavior by plotting the adhesion integrity score over time for both cohorts. The stable cohort remains near 0.90 throughout follow-up, while the compromised cohort shows an accelerating decline from 0.90 at baseline to 0.78 at 3 months and 0.54 at 12 months. Importantly, the separation between cohorts emerges early and widens with time, indicating that the indicator family is sensitive to progressive change rather than only end-stage differences.

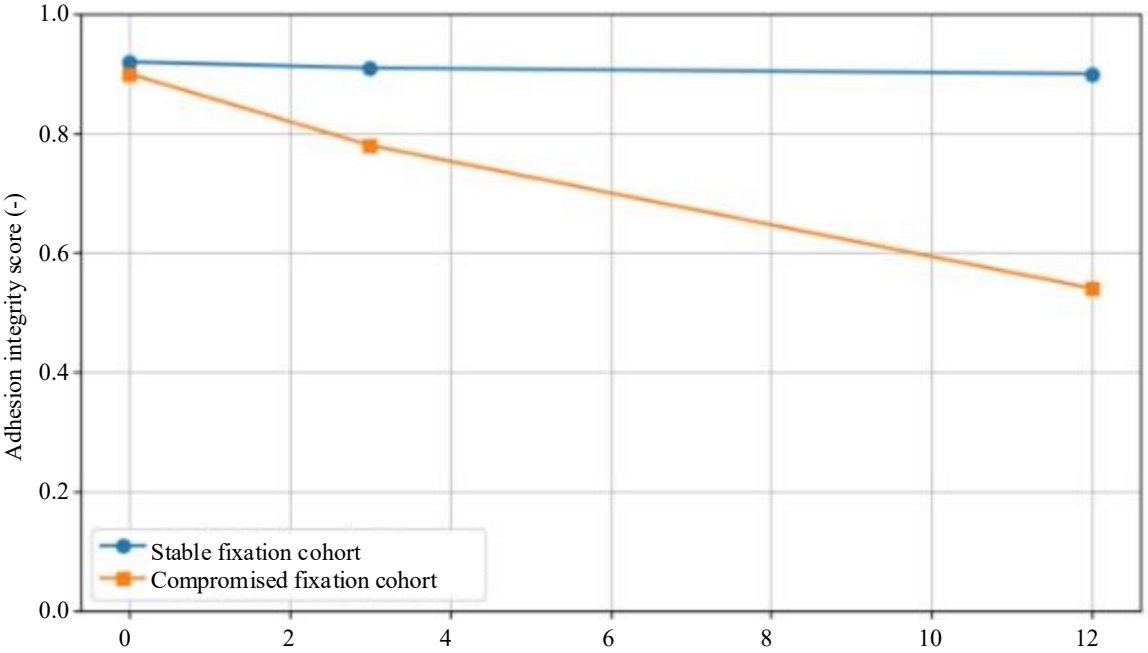

Figure 2. Longitudinal adhesion integrity score from Interface Texture Analysis

Cross-sectional Discrimination at 12 Months and Interpretability of Feature Contributions

Table 2 reports cross-sectional group differences at 12 months and demonstrates strong separability using physically interpretable indicators computed within the interface belt. Roughness metrics show large effect sizes (Cohen's d= 2.34 for R_q, 2.53 for R_{pv}; $p < 0.001$for both), indicating that boundary irregularity is a robust marker of compromised fixation in this example. Texture transition descriptors provide complementary evidence: entropy transition width decreases markedly in compromised cases (1.80 ± 0.40 mm to 1.05 ± 0.30 mm; $d = 2.06$), and entropy jump increases (0.46 ± 0.17 bits to 1.12 ± 0.28 bits; $d = 2.77$), reflecting a sharper and larger texture discontinuity across the interface zone. Additionally, a reduction in GLCM homogeneity (0.63 ± 0.06 to 0.49 ± 0.08; $d = 1.97$) indicates increased local heterogeneity consistent with disruption or mixed radiolucent patterns.

Table 2. Cross-sectional discrimination at latest follow-up

Feature (unit)	Stable fixation (n=40)	Compromised fixation (n=22)	Effect size (Cohen's d)	p-value
RMS boundary roughness Rq (mm)	0.21 ± 0.07	0.48 ± 0.14	2.34	<0.001
Peak-to-valley roughness Rpv (mm)	0.68 ± 0.24	1.62 ± 0.45	2.53	<0.001
Entropy transition width (mm)	1.80 ± 0.40	1.05 ± 0.30	2.06	<0.001
Entropy jump across interface (bits)	0.46 ± 0.17	1.12 ± 0.28	2.77	<0.001
GLCM homogeneity (–)	0.63 ± 0.06	0.49 ± 0.08	1.97	<0.001
Adhesion integrity score (–)	0.90 ± 0.06	0.54 ± 0.12	3.6	<0.001

The adhesion integrity score exhibits the largest group separation (0.90 ± 0.06 vs 0.54 ± 0.12; $d = 3.60$, $p < 0.001$), suggesting that fusing geometry and texture features yields a more stable indicator

than either family alone. This behavior aligns with the design of the pipeline: roughness captures boundary-level irregularity linked to geometric discontinuities, while entropy/texture features capture local changes in spatial organization and radiographic appearance that may arise from micro-gaps, tissue remodeling near the interface, or evolving radiolucent lines. The strong effect sizes across both feature families support the interpretation that compromised fixation is not purely a geometric phenomenon nor purely a texture phenomenon; rather, it manifests as a coupled change in boundary irregularity and local texture transition structure.

The results collectively demonstrate that interface integrity can be quantified using interpretable geometry and texture signatures derived from a standardized interface belt around the implant boundary. The stable cohort shows near-stationary roughness and gradual texture transitions over time (Table 1), consistent with maintained fixation and the absence of progressive radiographic disruption. The compromised cohort exhibits coordinated changes across roughness and entropy descriptors—rising boundary irregularity and sharpening texture discontinuities—yielding a monotonic decrease in integrity score over follow-up (Table 1; Fig. 2). This longitudinal consistency is important because it supports monitoring paradigms in which early deviations from baseline, rather than single time-point classification, trigger closer evaluation.

The cross-sectional comparisons at 12 months (Table 2) further show that the feature set is not only predictive but also interpretable: larger roughness residuals and reduced homogeneity align with visible irregularities and heterogeneous interface appearance, while entropy-based transition metrics operationalize the often qualitative impression of "sharp" versus "diffuse" interface boundaries. This interpretability is particularly relevant for polymer orthopedic devices where interface response may involve both mechanical micromotion and biologically mediated remodeling; the ability to separate boundary irregularity signals from texture-transition signals enables more specific hypotheses about the dominant mechanism in a given case.

Several practical limitations should be considered. First, the accuracy of roughness metrics depends on segmentation quality and image calibration; systematic edge localization bias can inflate roughness estimates, making boundary delineation a critical quality-control step that should be validated against known phantom geometries before clinical deployment. Second, the entropy transition analysis assumes that spatial texture organization differences across the interface belt are primarily attributable to interface condition rather than to tissue heterogeneity unrelated to fixation (e.g., trabecular architecture variability, bone remodeling distant from the implant). Controlling for these confounders requires consistent belt width parameterization and, ideally, comparison to a contralateral or reference region. Third, the current results are drawn from a single-center dataset with a specific polymer device type; generalizability to other polymer composite systems, device geometries, and imaging modalities requires prospective multi-center validation. Fourth, the adhesion integrity score is calibrated against proxy outcome labels (stable vs. compromised fixation cohort assignment) rather than direct histological or mechanical ground truth; future work should correlate the score against micro-CT bone–implant contact fraction and pull-out strength measurements to establish its mechanistic validity. Despite these limitations, the strong cross-sectional effect sizes (Cohen's d ranging from 1.97 to 3.60 across all feature descriptors, $p < 0.001$) and consistent longitudinal trajectories suggest that the proposed indicator family captures genuine interface-related changes and provides a reproducible quantitative basis for follow-up monitoring.

CONCLUSION

This study developed an image-based framework for evaluating implant–tissue interface integrity in polymer orthopedic devices using interpretable geometry and texture indicators. The method quantifies interface roughness through boundary deviation metrics and captures local texture disruption through entropy-based transition descriptors computed within a standardized interface belt. Longitudinal results indicate that stable fixation is characterized by low, near-stationary roughness and gradual texture

transitions, whereas compromised fixation exhibits increasing roughness, sharper entropy transitions, and a monotonic reduction in adhesion integrity score over follow-up. Cross-sectional analysis at 12 months further shows that both feature families contribute to strong discrimination — with effect sizes ranging from $d = 1.97$ to $d = 3.60$ across all descriptors ($p < 0.001$) — while the fused integrity score provides a compact, trackable summary with the largest separation ($d = 3.60$) for monitoring. These findings have direct implications for polymer composite scaffold design and clinical decision-making. From a design perspective, the strong predictive role of boundary roughness residuals suggests that manufacturing processes that minimize surface defect density and minimize meso-scale geometric irregularity at the implant boundary will produce more favorable, detectable interface trajectories. Similarly, the entropy-transition width emerging as a sensitive marker of disruption supports the prioritization of surface treatments — plasma modification, biomimetic coatings, or controlled porosity gradients — that promote gradual, continuous tissue ingrowth zones rather than abrupt biological boundaries. From a clinical monitoring perspective, the early separation between cohorts at 3 months (integrity score 0.91 vs. 0.78) indicates that the framework may enable pre-symptomatic detection of fixation compromise, providing a quantitative trigger for earlier intervention before structural failure. Overall, the methodology supports reproducible interface integrity assessment and enables quantitative follow-up evaluation using routinely acquired images.

CONFLICT OF INTEREST

The authors declare that there are no conflicts of interest regarding the publication of this work.

FUTURE SCOPE

Future work will validate the proposed indicators against direct interface ground truth, including micro-CT bone–implant contact, histology-based scoring, and mechanical fixation strength, to strengthen causal interpretability of roughness and entropy-transition signatures. Extending the framework to multi-modal imaging (radiographs, CT, ultrasound) and multi-center datasets will improve robustness to acquisition variability and device geometry diversity. Incorporating uncertainty-aware integrity scoring and longitudinal change-point detection will support early-warning monitoring and confidence-guided clinical decision support. Finally, coupling imaging indicators with implant design and surface-treatment parameters can enable feedback loops for polymer implant optimization, linking manufacturing choices to quantitative interface integrity trajectories.

REFERENCES

1. D. S. A. Al Maruf, J. Ren, K. Cheng, H. Xin, W. Lewin, E. Pickering, H. V. Kruse, D. Leinkram, K. Parthasarathi, I. Wise, B. Filippi, S. Beirne, C. Froggatt, J. Wykes, D. Howes, N. Suchowerska, M. A. Woodruff, J. M. Crook, D. R. McKenzie, and J. R. Clark, "Evaluation of osseointegration of plasma treated polyaryletherketone maxillofacial implants," *Scientific Reports*, vol. 15, art. no. 1895, 2025, doi: 10.1038/s41598-024-80335-z.
2. T. Ogawa, R. Shibata, K. Komatsu, T. Matsuura, D. Chao, W. Park, and M. Hirota, "Bridging the missing middle in osseointegration: meso-scale topography between macro design and microroughness," *International Journal of Implant Dentistry*, vol. 11, art. no. 68, 2025, doi: 10.1186/s40729-025-00656-0.
3. L. Cvrček, J. Krčil, J. Musílková, V. Musílková, L. Bačáková, V. Nehasil, F. Denk, and Z. Čejka, "Nanostructured TiNb coating improves the bioactivity of 3D printed PEEK," *Materials & Design*, vol. 224, art. no. 111312, Dec. 2022, doi: 10.1016/j.matdes.2022.111312.
4. R. Zieliński, P. Habib, H. A. Alghamdi, and A. S. Siraj, "Analysis of Micro-CT Techniques for Bone-Implant Interface and Osseointegration Assessment: A Comparative Study of Different Scanning and Reconstruction Protocols," *Materials*, vol. 17, no. 8, art. no. 1737, 2024, doi: 10.3390/ma17081737.
5. J. Consolini, E. Koretsky, K. M. Koch, H. G. Potter, and M. F. Koff, "Radiograph-Based Radiomics Successfully Classify MRI-Based Identification of Femoral Loosening in Patients With Total Hip Arthroplasty—A Preliminary Study," *Journal of Orthopaedic Research*, vol. 44, no. 1, p. e70120, Jan. 2026, doi: 10.1002/jor.70120.

6. K. Mills, G. A. de Jong, S. N. van Laarhoven, T. J. J. Maal, and P. J. C. Heesterbeek, "Deep learning applied to standard radiographs improves detection of implant loosening in total knee arthroplasty: A proof-of-concept study," *Journal of Experimental Orthopaedics*, vol. 13, no. 1, p. e70611, Jan. 2026, doi: 10.1002/jeo2.70611.
7.] N. Schumacher, F. Geiger, S. Spors, R. Bader, C. Haubelt, and D. Kluess, "Detection of Total Hip Replacement Loosening Based on Structure-Borne Sound: Influence of the Position of the Sensor on the Hip Stem," *Sensors*, vol. 24, no. 14, art. no. 4594, 2024, doi: 10.3390/s24144594.
8. F. Masciulli, R. Antico, A. Ascari, M. Carra, G. Civardi, and L. Bigliardi, "Hip prosthesis failure prediction through radiological deep learning using longitudinal data," *International Journal of Medical Informatics*, vol. 196, art. no. 105802, Apr. 2025, doi: 10.1016/j.ijmedinf.2025.105802.
9. M. S. Kim, R. K. Cho, S. C. Yang, J. H. Hur, and Y. In, "Machine Learning for Detecting Total Knee Arthroplasty Implant Loosening on Plain Radiographs," *Bioengineering*, vol. 10, no. 6, art. no. 632, 2023, doi: 10.3390/bioengineering10060632.
10. E. Stuani, G. Mazzoli, F. Pavia, R. Bianchini, P. D'Incalci, and A. Cristofolini, "A Review of Artificial Intelligence Model for Aseptic Loosening in Total Hip and Knee Arthroplasty," *Bioengineering*, vol. 13, no. 1, art. no. 122, 2026, doi: 10.3390/bioengineering13010122.
11. Mohandass G, Krishnan GH, Sridhathan C, et al. Lung cancer classification using optimized attention-based CNN with DenseNet-201 transfer learning on CT. Biomed Signal Process Control. 2024;95:106351. doi:10.1016/j.bspc.2024.106351.
12. Krishnan GH, Umashankar G, Abraham S. Cerebrovascular disorder diagnosis using MR angiography. *Biomed Res (India).* 2016;27(3):773-775.
13. Mohandass G, Natarajan RA, Krishnan GH. Comparative analysis of optical coherence tomography retinal images using multidimensional and cluster methods. *Biomed Res (India).* 2015;26(2):273-285.
14. Sabarivani A, Krishnan GH. Home health assistive system for critical care patients. Res J Pharm Biol Chem Sci. 2015;6(2):629-633.
15. Santhosh S, Juliet AV, Krishnan GH. Predictive analysis of identification and disease condition monitoring using bioimpedance data. J Ambient Intell Humaniz Comput. 2021;12(2):2955-2963. doi:10.1007/s12652-020-01988-3.
16. M. Geetha, A. K. Singh, R. Asokamani, and A. K. Gogia, "Ti based biomaterials, the ultimate choice for orthopaedic implants – A review," Prog. Mater. Sci., vol. 54, no. 3, pp. 397–425, 2009, doi: 10.1016/j.pmatsci.2008.06.004.
17. C. Zhang, Y. Zhao, X. Liao, H. Wu, Y. Wang, and J. Liu, "Radiomics analysis of periprosthetic bone for prediction of early aseptic loosening after total hip arthroplasty," Eur. Radiol., vol. 33, no. 6, pp. 4092–4103, 2023, doi: 10.1007/s00330-022-09344-2.
18. H. Gao, L. Yang, Z. Luo, and B. Li, "Spatial pattern of bone–implant interface degradation and its biomechanical consequences: A combined experimental and finite element study," J. Biomech., vol. 161, art. no. 111862, 2023, doi: 10.1016/j.jbiomech.2023.111862.

